

JGR Space Physics

RESEARCH ARTICLE

10.1029/2018JA026244

Key Points:

- Deuterium (D) emissions from the limb of Mars are analyzed to produce atomic abundances and escape rate estimates in the upper atmosphere
- D property variations are pronounced. Brightness and densities increase with Mars' proximity to the Sun and peak near southern summer solstice
- Variations of deuterium brightness, densities, and escape rates suggest a seasonally varying D/H ratio at Mars

Supporting Information:

- Supporting Information S1

Correspondence to:

M. Mayyasi,
majdm@bu.edu

Citation:

Mayyasi, M., Clarke, J., Bhattacharyya, D., Chaufray, J. Y., Benna, M., Mahaffy, P., et al. (2019). Seasonal variability of deuterium in the upper atmosphere of Mars. *Journal of Geophysical Research: Space Physics*, 124, 2152–2164. <https://doi.org/10.1029/2018JA026244>

Received 29 OCT 2018

Accepted 2 FEB 2019

Accepted article online 17 FEB 2019

Published online 20 MAR 2019

Seasonal Variability of Deuterium in the Upper Atmosphere of Mars

Majd Mayyasi¹ , J. Clarke¹ , D. Bhattacharyya¹ , J. Y. Chaufray² , M. Benna³, P. Mahaffy³ , S. Stone⁴ , R. Yelle⁴ , E. Thiemann⁵ , M. Chaffin⁵ , J. Deighan⁵ , S. Jain⁵ , N. Schneider⁵ , and B. Jakosky⁵ 

¹CSP, Boston University, Boston, Massachusetts, USA, ²LATMOS, CNRS/UPMC/UVSQ, Paris, France, ³NASA Goddard Space Flight Center, Greenbelt, Maryland, USA, ⁴LPL, University of Arizona, Tucson, Arizona, USA, ⁵LASP, University of Colorado Boulder, Boulder, Colorado, USA

Abstract Measurements by multiple Mars Atmosphere and Volatile Evolution mission instruments, obtained between November 2014 and November 2017, are analyzed to produce deuterium properties in the upper atmosphere of Mars. We show here, for the first time, the seasonal distribution and variability of D densities, temperatures, and estimated Jeans escape rates at the exobase (200 km). Within the data constraints, it is found that the variations in D properties are similar for the northern and southern hemispheres, and peak near southern summer solstice. Trends in the D Lyman- α brightness, temperature, density, and escape rate are increasing during the beginning of the dust storm season, peak near southern summer solstice, and decrease toward the end of the dust storm season. This suggests that seasonal drivers at Mars cause deuterium in the upper atmosphere to become globally enhanced when Mars is closest to the Sun and during the Martian dust season when water is provided to the upper atmosphere by subsurface, hydrological, and dust storm dynamics.

Plain Language Summary Water escape at Mars can be examined by analyzing the properties of present day hydrogen and its isotope deuterium. The ratio of the abundance of these two atoms at the upper atmosphere of Mars can provide limitations to the preferential escape of one over the other and can provide information on the present rate of escape of water from the upper atmosphere. The results from this work can be paired with estimates of what early Mars and the Sun were like in order to provide estimates for the early water content on ancient Mars. In this paper, the most comprehensive set of observations of deuterium from Mars are analyzed, and the resulting properties of deuterium in the upper atmosphere of Mars are presented.

1. Introduction

Estimates of the ancient water content at Mars derived from surface mineralogy are presently debated (e.g., Bibring et al., 2006; Head et al., 2003). Recent ground-based, orbital, and in situ observations have been used to re-evaluate water reservoirs on the Martian surface and in the lower atmosphere in order to better determine global water loss (Fedorova et al., 2018; Mahaffy et al., 2015; Orosei et al., 2018; Smith et al., 2009; Trokhimovskiy et al., 2015; Villanueva et al., 2015). These determinations are made by constraining present epoch estimates that range from few to tens of meters to an integrated ancient reservoir of ~140-m global equivalent layer of water (e.g., Jakosky et al., 2018).

The isotopic ratio of deuterium (D) to hydrogen (H) abundance at Mars has been useful for describing the planet's early formation (Fisher, 2007; Horner et al., 2009; Solomon et al., 2005). Directly measured and inferred ratios of D to H abundances (D/H) have been used to quantify water in the various ice and vapor reservoirs on the surface, within the subsurface, and throughout the lower atmosphere (Bertaux & Montmessin, 2001; Kass & Yung, 1999; Krasnopolsky, 2000; Montmessin et al., 2005; Owen, 1992). Derivations of the Martian D/H ratio and comparisons with terrestrial values have been used to estimate the integrated loss rate of H, and subsequently to constrain water loss from Mars (e.g., Jakosky et al., 2018; Krasnopolsky, 2002; Villanueva et al., 2015; Yung et al., 1988, and references therein).

The upper atmosphere of Mars is the region where escape into outer space occurs (Carr, 1986; Lammer et al., 2013). Determining the present escape rate of water and its variability in the upper atmosphere can therefore be used to extrapolate past values and to constrain estimates of primordial water abundance on the Martian

surface. To this purpose, roving and orbiting missions at Mars are being used to characterize the planet's climatology using a variety of techniques, such as determining the atmospheric abundance of species and their isotopes (Ehlmann & Edwards, 2014; Gillmann et al., 2011; Jakosky et al., 1994, 2017).

Atomic hydrogen in the upper atmosphere of Mars originates from photo-dissociated water lower in the atmosphere. Through chemical reactions and hydrological cycle dynamics, water-based atomic H and D are transported to the upper atmosphere where they can escape. Early theories set the time scale for this transport to be on the order of tens of years (Hunten & McElroy, 1970). However, observations by the Hubble Space Telescope as well as Mars-orbiting spacecraft have shown the planet to have an extended H corona with properties that varied on shorter (seasonal) time scales than theoretically predicted (Bhattacharyya et al., 2015; Chaffin et al., 2014; Chaffin et al., 2015; Chaffin et al., 2017; Chaufray et al., 2015; Clarke, 2018; Clarke et al., 2014; Halekas, 2017; Heavens et al., 2018). These variations in brightness are consistent with variability in lower atmospheric water vapor and HDO observed at Mars (Fedorova et al., 2018; Villanueva et al., 2015).

Properties of H and D in the upper atmosphere of Mars can vary due to both external mechanisms such as space weather and solar activity as well as internal ones such as dust dynamics and atmospheric circulation (Mayyasi et al., 2017; Mayyasi et al., 2018). The time scales for these internal and external processes range from hours to months. Measuring properties of D and H over a baseline in time that exceeds the variability of individual physical processes is therefore fundamental to interpreting the dynamical nature of water escape where species are most volatile. The Mars Atmosphere and Volatile Evolution (MAVEN) mission has been in orbit about Mars since September 2014 (Jakosky, 2015). MAVEN carries a high-resolution echelle channel, designed to resolve Lyman- α emissions from H and D at 121.567 and 121.534 nm, respectively, as well as other emissions (Clarke et al., 2017; Mayyasi et al., 2017; McClintock et al., 2015).

A comprehensive analysis of the properties of D in the upper atmosphere of Mars—the interface of loss to space—have so far been missing from the context of H variability and are critical in determining the D/H ratio. The MAVEN mission has been designed for such an analysis of D and H properties. In this work, three Earth years of echelle observations are used to map the properties of atmospheric D at Mars with unprecedented coverage. The optically thin D Lyman- α emission is analyzed and used with independent temperature derivations to provide modeled estimates of density and escape rates in order to provide insights into D/H and its variability.

A description of the MAVEN instruments used in this study is provided in section 2. The models used to simulate the observations are described in section 3. Resulting brightness values, derived densities, and escape rates for deuterium at Mars are shown in section 4. Discussion and interpretation of the results is presented in sections 5 and 6, respectively. Additional information showing consistent results for various modeling assumptions and observational details are provided in the supporting information.

2. Instruments and Observations

Observations from three MAVEN instruments were used in this work: the remote sensing Imaging and Ultraviolet Spectrograph (IUVS), the in situ Neutral Gas and Ion Mass Spectrometer (NGIMS), and the Extreme Ultraviolet Monitor (EUVM) instruments. Measurements were separated into two seasonal epochs: aphelion (where solar longitude, L_s , varies between 0° and 120°) and perihelion (where L_s varies between 220° to 340°). Details on the observations are provided in the supporting information.

2.1. IUVS

Observations early in the MAVEN mission defined the background noise threshold on the IUVS detector and showed that the few months around perihelion were optimal for observing faint emissions such as D (Mayyasi, Clarke, Quénerais, et al., 2017). IUVS makes separate observations of the planet's disk, limb, and corona with each orbit. The D emissions appear brightest at the sunlit limb-pointed line of sight due to limb brightening of the optically thin emission. We therefore concentrate exclusively on these limb observations for deriving a brightness profile for D. In order to obtain an altitude profile of deuterium emissions, only observations where the minimum ray height was between the surface and 300 km were used. The deuterium signal above 300 km is too faint to be detected (Mayyasi, Clarke, Bhattacharyya, et al., 2017).

Resulting echelle spectra were reduced and calibrated at Lyman- α wavelengths to derive the D brightness in standard units of Rayleighs (Mayyasi, Clarke, Quénerais, et al., 2017).

2.2. NGIMS

NGIMS makes in situ measurements of neutral and ion densities (Mahaffy et al., 2014). The neutral densities of species with masses ranging between 2 and 150 amu are measured in each nominal MAVEN orbit along inbound and outbound segments of the spacecraft track. Only inbound observations are used here due to adsorption of gas onto the walls of the spectrometer that affect measurements in the outbound orbital segments (e.g., Cui et al., 2009). MAVEN periapsis altitudes reach ~ 150 km during nominal orbits and can drop to ~ 130 km during select, for example, “deep dip” campaigns (Benna et al., 2015). In the observations used here, nominal orbits were used. NGIMS data are used to derive neutral temperature values at the exobase (the altitude where the mean free path equals the scale height, taken here to be 200 km). CO_2 , N_2 , and Ar are the most chemically stable species measured by NGIMS (Mahaffy, Webster, et al., 2015). In this work, the neutral densities of CO_2 and Ar were used to calculate scale heights in order to provide a temperature in a given altitude range. The methodology for this derivation is described further in section 3. Observations spanning aphelion and perihelion were used to constrain temperatures in the upper atmosphere of Mars.

2.3. EUVM

MAVEN carries an Extreme Ultraviolet Monitor (EUVM) instrument (Eparvier et al., 2015) that makes measurements of the solar energy incident at Mars using three wavelength channels. Two channels are dedicated to obtaining X-ray irradiances at 0.1–3- and 0.1–7-nm wavelengths, and one channel is dedicated to isolating the solar Lyman- α line at 121.6 nm. EUVM measurements of the solar Lyman- α flux at Mars are used in the modeling component of this analysis, described below, to determine the concentrations of deuterium from the observed irradiances. EUVM observations that were made on the days of the echelle observations were used to provide the solar irradiance at Mars. In this work, observations from IUVS, NGIMS, and EUVM are averaged for relatively long periods of time, and span over 1.5 Mars years.

3. Models

In order to derive physical properties from the observed D brightness, we use a single-scattering model, adapted for optically thin emissions (Bhattacharyya et al., 2017). Procedurally, these model simulations require constraining ambient atmospheric conditions at the times of the observed emissions in order to obtain the concentrations of the emitting species along a given line of sight. The single-scattering model utilized had previously assumed spherical symmetry for simplicity. To make model retrievals of the observations presented here more physically plausible, a spherically asymmetric background atmosphere is adopted, where the asymmetry is assumed to be due to variations in solar zenith angle (SZA) and Martian season, denoted by solar longitude, L_s . SZA depends on both latitude as well as local time and is chosen as the single parameter to represent variations in planetographic observational conditions. Therefore, in this application, a single-scattering model is coupled to a 2-D background atmospheric model that includes empirically derived neutral densities and temperatures, to provide a global map of conditions that can be used to reproduce the observed emission brightness for D. Aphelion and perihelion scenarios were considered to account for seasonal variations at Mars.

Below 80 km, the predominantly CO_2 atmosphere of Mars absorbs almost all Lyman- α emission, and no emissions are expected to be generated at those altitudes (Bhattacharyya et al., 2017). At thermospheric altitudes (above 80 km), a global asymmetric background atmosphere is simulated using the following methodology: (1) scale heights of CO_2 and Ar, obtained from NGIMS density profiles, are used to determine a neutral atmospheric temperature near exobase altitudes of ~ 200 km. (2) Empirically derived trends are used to account for variability in the exobase neutral temperature with SZA and season. (3) A mathematical representation is used to generate a temperature profile for remaining thermospheric altitudes. (4) A CO_2 atmosphere is derived from the neutral temperature using an atmospheric model and constrained to NGIMS density observations, at overlapping altitudes, for consistency. (5) Finally, a single-scattering model uses the asymmetric background atmosphere, as well as IUVS observations, to simulate the D intensity for comparison with the IUVS observations to produce a best fit exobase density.

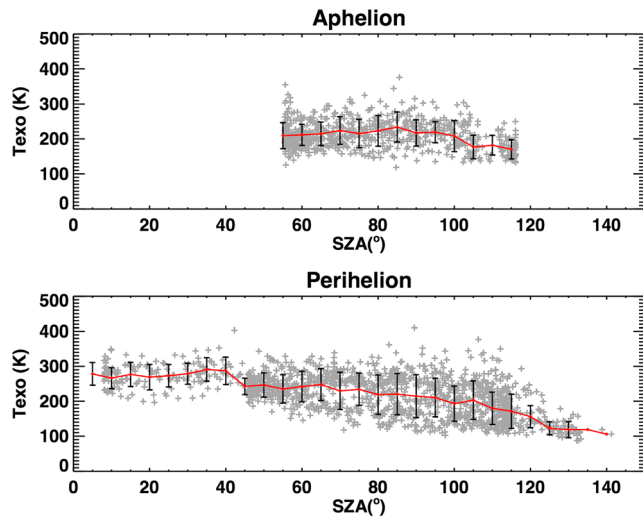


Figure 1. Neutral temperatures derived from NGIMS observed scale heights for orbits at (top) aphelion and (bottom) perihelion conditions. Individual orbit temperatures are shown as gray plus symbols and span a range of SZAs. The red lines in each panel show trends from 5° SZA bins. Black vertical lines represent the standard deviation within each bin.

3.1.2. Determining Seasonal and SZA Variations in Exobase Temperature

The averaged CO₂ and Ar scale height-derived temperatures are shown in Figure 1 for aphelion and perihelion seasons. During aphelion, NGIMS nominal in situ measurements spanned ~50° to 110° SZA. During both perihelion seasons observed by MAVEN to date, NGIMS measurements spanned ~5° to 140° in SZA. The red horizontal lines are the averages of values in 5° SZA bins, with their standard deviation in vertical black error bars. At the common SZA of 50° for each season, aphelion and perihelion temperatures were 210 ± 37 and 235 ± 40 K, respectively.

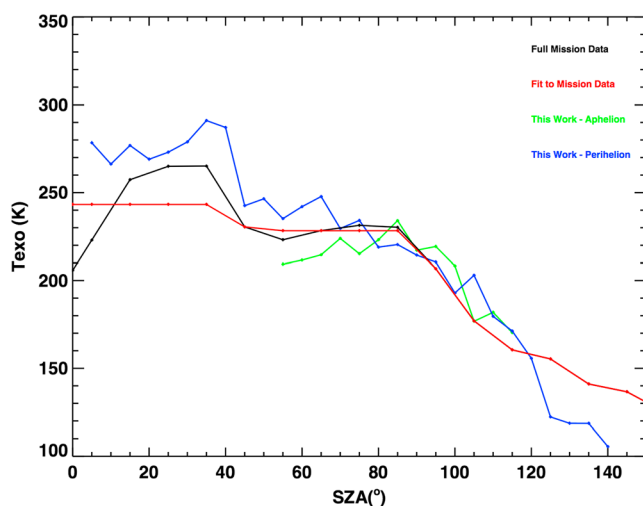


Figure 2. A comparison of exobase temperature variability with SZA for specific seasons and for all seasons across the MAVEN mission. NGIMS observations at aphelion are shown in green, binned by 5° in SZA, and perihelion observations are shown in blue with similar SZA binning. Observations from the first 1.75 years of the MAVEN mission are shown in black and fit to a curve shown in red (Stone et al., 2018).

3.1.1. Obtaining Temperatures of the Martian Atmosphere at the Exobase

In a horizontally stratified atmosphere, the altitude over which the density of a species decreases by e^{-1} of its value at some reference altitude is defined as the scale height, H_n , and is defined as

$$H_n = \frac{k_b T_n}{m_n g_r} \quad (1)$$

where k_b is the Boltzmann constant, T_n is the neutral temperature, m_n is the mass of the neutral species n , and g_r is the gravity at the altitudes of the measurements.

For the observations used here, MAVEN spacecraft periapsis nominally ranged between ~150 and 180 km. The slope of NGIMS CO₂ and Ar densities between 160 and 200 km were used to derive a scale height for each species. In cases where the spacecraft periapsis was higher than 150 km, the slope of the densities between 180 and 220 km was used. Using equation (1), the neutral temperature was calculated for each species. The temperatures derived using this method showed results similar to within ~10% for aphelion, and ~15% for perihelion, for each species. Since these differences were within the uncertainties in the measurements, an average temperature from the two species was adopted as a representative exobase temperature.

There have been ongoing efforts to characterize the neutral upper atmospheric temperature at Mars (Bougher et al., 2017; Stone et al., 2016; Stone et al., 2018). In order to get a broader SZA representation of the neutral temperature variation at the exobase, the seasonal trends obtained here from NGIMS-constrained scale heights are compared to trends of empirically constrained MAVEN observations that span the whole mission and are shown in Figure 2. The NGIMS measurements available at any time are for one location only. This necessitates determining a time-averaged functional relationship for the global representation of temperature variation with SZA. Local time variations in exobase neutral temperatures are within the uncertainties of the mission-long averages and are not accounted for separately.

The temperatures derived using the method described here are consistent with those obtained independently and follow similar trends to observations across the MAVEN mission (Stone et al., 2016, 2018). The trend lines fit to the full mission observations are used to extrapolate the exobase temperatures to remaining SZAs not covered by NGIMS during the IUVS observation times analyzed in this work. An additional temperature shift is done (incremental for aphelion temperatures and decremental for perihelion temperatures) to the fit trend line to account for seasonal variations in exobase temperatures. The resulting aphelion and perihelion temperatures extracted from this interpolation and scaling are 216 ± 39 and 255 ± 29 K, respectively, at the subsolar point (0° SZA).

Linear interpolations of these values were used to constrain the exobase temperature of the Martian atmosphere at 0° SZA (overhead Sun conditions) for other solar longitude observations.

3.1.3. Determining Temperature Profiles With Altitude

For the seasonal and SZA conditions of the observations, the neutral temperature, determined at the exobase, was used to generate a profile at thermospheric altitudes. This was done using a mathematical representation (Krasnopolsky, 2002):

$$T(h) = T_{\infty} - (T_{\infty} - 125) \times \exp\left(-\frac{(h-90)^2}{11.4 \times T_{\infty}}\right) \quad (2)$$

where h is the altitude (in km) between 90 and 400 km and T_{∞} is the exospheric temperature (in degrees Kelvin) derived from the NGIMS neutral density-scale heights. The neutral temperature is assumed to remain isothermal above the exobase (200 km) for a particular SZA.

3.1.4. Generating a Consistent Neutral Atmosphere

CO₂, which is the dominant component of the Martian atmosphere, absorbs Lyman- α (e.g., Bertaux et al., 2006); therefore, a neutral background atmosphere consisting of CO₂ as well as D densities is required as input to the single-scattering model. The CO₂ abundance was generated from a volume mixing ratio at 80 km, and used the temperature provided by NGIMS measurements and molecular and eddy diffusion to account for interactions with other neutral species to provide a density profile for the altitudes of interest for the observing conditions (Matta et al., 2013).

The CO₂ mixing ratios at 80 km are consistent with the relative abundances found in the Mars Climate Database for CO₂ and did not show significant variability with SZA (Forget et al., 1999; Lewis et al., 1999). However, the pressure of the neutral atmosphere is variable and can introduce variability not quantified by the mixing ratio used. The density of the atmosphere at 80 km is a free parameter that was varied to constrain the modeled species with NGIMS-observed CO₂ densities near spacecraft periapsis for aphelion and perihelion conditions (Mayyasi et al., 2018). This methodology therefore provides an empirical density profile for CO₂ in the asymmetric background model that changes only with the neutral temperature.

Deuterium is a lighter species and varies differently with altitude than its heavier counterpart, CO₂ (e.g., Krasnopolsky, 2002). A density profile between the altitude limits where D emissions are most relevant (80 to 300 km) was needed for the single-scattering model input. Above the exobase altitude of 200 km, a modified Chamberlain approach, which accounts for the variation of temperature with SZA, was used (Vidal-Madjar & Bertaux, 1972). Between 120 and 200 km, a simple diffusion model was used (Chaufray et al., 2008). At the exobase, the D density was considered to be a free parameter with a range of 6 values discussed in the next section. A mathematical formulation ($nT^{5/2} = \text{constant}$, where n is the density of a light species and T is its temperature) first derived by Hodges & Johnson (1968) and recently verified by Yelle et al. (2018) for H atoms, was used to determine the SZA variability of D densities at the exobase. Below the assumed homopause at 120 km (Mahaffy et al., 2015; Nagy et al., 2009), a linear profile for D was used for simplicity, similar to that described in Bhattacharyya, Clarke, Bertaux, et al. (2017) and that was consistent with a diffusion-generated atmosphere.

3.1.5. Simulating D Densities From Observed and Modeled Intensities

A radiative transfer model described in Bhattacharyya, Clarke, Bertaux, et al. (2017), developed for interpreting the optically thick H Lyman- α observations, was modified to simulate the optically thin D emission in order to interpret the IUVS deuterium observations. D Lyman- α emissions at Mars are optically thin along a given line of sight where only single scattering is assumed. Since this D emission is due to solar resonant scattering, EUVM-measured solar Lyman- α flux is used to determine the intensity of the observed emission for a particular observation (Thiemann et al., 2017). The EUVM measurements of the line-integrated Lyman- α flux were converted to a line center flux in order to calculate the g value for the deuterium emission at Mars (Chaufray et al., 2008; Emerich et al., 2005). The g values range between 4.93 and 12.1×10^{-4} photons/s for the data analyzed here. The g values were then multiplied by a line of sight column density in the single-scattering model to simulate the intensity for deuterium emission at Mars.

Six exobase D densities were used to generate the D background atmosphere for each of the observing conditions. These densities were chosen to be 100, 500, 1,000, 3,000, 5,000, and 7,000 cm⁻³. Each of the six densities was used with the CO₂ background and NGIMS-constrained temperatures to provide a library of

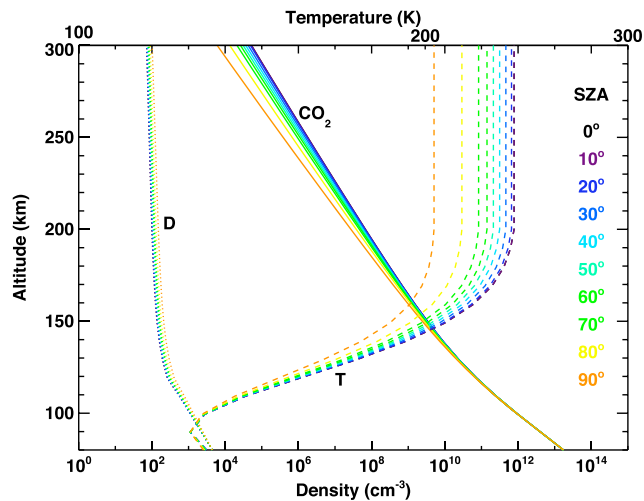


Figure 3. Background neutral atmosphere used in the single-scattering model to simulate D Lyman- α emissions and derive D densities. This atmosphere is generated for the average neutral temperature taken at perihelion derived from NGIMS observation for different SZA indicated by line color. The CO₂ density is shown in solid lines, and the D density is shown in dotted lines. Temperatures follow the top x axis scale and are shown in dashed lines.

atmospheres. The single-scattering model uses the solar flux measured at the time of each observation with this library of atmospheres to generate a set of emission profiles for each line of sight in the observations. The exobase density that corresponds to the emission profile that best fits the data is determined by minimizing chi-square deviations between data and model in a least squares fit. The uncertainty in the derived D density for a particular observation is determined by accounting for all modeled D densities that lie within the minimum chi-square +1 range.

A sample neutral atmosphere generated as background for the single-scattering model is shown in Figure 3. The D and CO₂ density profiles are adopted for an average temperature case at perihelion and use the 100-cm⁻³ exobase density value for D.

4. Results

The D Lyman- α emission is faint in comparison to H Lyman- α (Bertaux et al., 1984). Therefore, only observations with a local SZA between 0° and 90° were considered to ensure that the entire atmosphere was sunlit between the surface and 300 km. Over 20,000 echelle image frames of the Martian limb, measured across the observational time span used here, fit the dayside criteria. Echelle spectra are averaged across the observational data set in order to optimize the signal to noise when retrieving the faint D signal.

The data were binned according to the line of sight latitude, SZA, minimum ray height altitude (hereafter referred to as altitude), and L_s . The bins considered include two in latitude, ranging between 90°N and 30°N for northern hemisphere observations and 30°S to 90°S for southern hemisphere observations. Three SZA bins were considered, ranging between 30° and 75° with 15° spacing. Twenty-one bins in altitude were used ranging between 0 and 400 km with 20-km spacing. At the highest altitudes, D was too faint to be resolved and so only observations up to 300 km were used in the analysis. At aphelion, one representative L_s bin was used ranging between 0° and 120° (described further next). At perihelion, six L_s bins were used ranging between 220° and 340° with 20° spacing. Observations made in each of the bins were spectrally aligned to account for differences in detector operational binning schemes before co-adding (see Table A1 in Mayyasi, Clarke, Bhattacharyya, et al. (2017) for a description of detector binning schemes used throughout the MAVEN mission). Insufficient echelle observations were available at equatorial regions (30°S to 30°N latitudes), lower SZAs (0°–30°), and L_s values beyond those considered here to build statistically significant brightness profiles due largely to the geometry of the MAVEN orbit. However, at the time of this writing, MAVEN continues to make echelle observations as Mars approaches perihelion. The next few months of observations would be used in future work to close existing observational gaps.

4.1. Aphelion

The first detections of Martian D emission based on Hubble Space Telescope observations showed Lyman- α brightness values of 30 Rayleigh (Bertaux et al., 1993) and 23 ± 6 Rayleigh (Krasnopolsky et al., 1998). These observations occurred at times when Mars was at 63° and 67° L_s , respectively, and therefore close to Mars aphelion (71° L_s). D and H Lyman- α emissions observed by MAVEN were found to vary dramatically throughout a Martian year and showed consistency with these previous detections (Clarke et al., 2017; Mayyasi, Clarke, Bhattacharyya, et al., 2017). Due to the faintness of the D signal near perihelion, and the limitations of the instrument, the D emission was not always attainable above the background detector noise. Aphelion observations between 0° and 120° L_s were co-added to improve signal to noise yet still fell below the detection limits. An example is shown in Figure 4 for one line of sight bin for reference and demonstrates the resolvability of D emission above the blueward wing of the H emission. The D emission signal is comparable to the background when near aphelion and more clearly resolvable (with fewer individual observations) near perihelion. Co-added observations from all available dayside aphelion observations are therefore used to provide an upper limit for the simulated properties. Using the average aphelion exobase

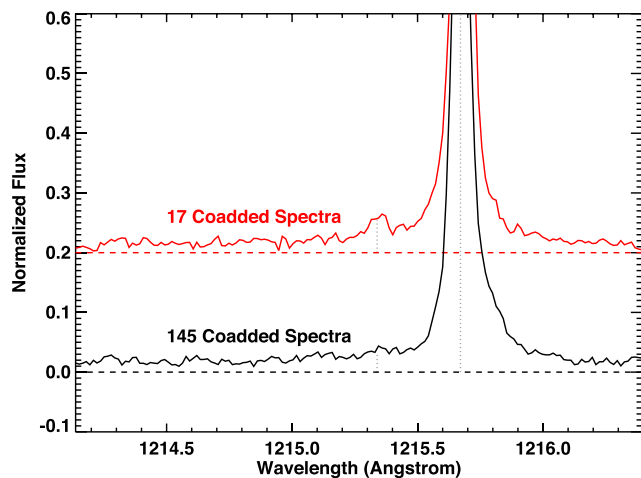


Figure 4. Sample spectra from aphelion (black) and perihelion (red) that correspond to bins of 60° – 75° SZA and 120–140-km altitude obtained from observations of the northern hemisphere of Mars. The aphelion spectrum is obtained by averaging 145 available integrations obtained between 60° and $80^{\circ} L_s$. The perihelion spectrum is obtained by averaging 17 available integrations between 220° and $240^{\circ} L_s$. The vertical dotted lines represent the locations of the D and H Lyman- α emission wavelengths at 1,215.34 and 1,215.67 Å, respectively. Both spectra are normalized in flux and the perihelion spectrum is vertically offset by 0.2 to facilitate comparison of the relative brightness of the D emission at each seasonal epoch. The asymmetry in the aphelion (black) H profile is due to the interplanetary hydrogen emission that is shifted red ward of the Mars H emission for these observations.

temperature of 216 K, the exobase density range and mean Jeans' escape rate for overhead Sun conditions are derived. The upper limits for the deuterium exobase density and escape rates at aphelion conditions are found to be $2.3 \pm 2.3 \times 10^3 \text{ cm}^{-3}$ and $\sim 3 \times 10^3 \text{ atoms}\cdot\text{cm}^{-2}\cdot\text{s}^{-1}$, respectively.

4.2. Perihelion

Mars perihelion occurs at $251^{\circ} L_s$. Observations spanning a range of 220° to $340^{\circ} L_s$ were analyzed to provide D brightness profiles for near-perihelion conditions at the L_s and SZA binning scheme described previously. Only bins with at least three observed spectra and that resulted in profiles with data points in at least five altitude grids were used. The resulting D irradiance from co-added observations as well as the model best fits are shown in Figure 5 for the averaged perihelion derived temperature of 255 K, and are sorted by hemisphere, L_s , and SZA. Data-model comparisons at the lower and higher temperature limits from the uncertainty in perihelion temperatures (226 and 284 K) are shown in Figures S1 and S2, respectively, in the supporting information, as are the number of observations used in each bin (Table S5).

The D densities at the exobase, derived by the single-scattering model from best fits to the irradiance data, and constrained to empirically determined exobase temperatures are listed in Table 1. The data cover observations made over a range of SZA. Subsequently, the asymmetric model utilizes a range of neutral temperatures. The range of solar conditions applicable to the echelle observations in each bin contribute to the uncertainties in the model-determined densities. To facilitate comparisons, the exobase densities and temperatures derived for D from different SZAs are extrapolated to 0° SZA (overhead Sun conditions) and are also shown in

Table 1. These results correspond to an asymmetric background model that adopts the average perihelion temperature of 255 K derived from NGIMS measurements. Similar results derived from the lower and higher perihelion temperature limits of 226 and 284 K are shown in Tables S1 and S2, respectively, in the supporting information.

The resulting D exobase densities, extrapolated to subsolar point conditions (SZA = 0°) for perihelion observations, are shown in Figure 6. The uncertainties in the modeled values stem from the ranges in the L_s , SZA, and altitude bins, and account for the range of results from model fits where more than one altitude profiles (at different SZA bins) were available for interpolation to subsolar point conditions. Figure 6 utilizes the averaged perihelion temperature of 255 K. Similar results corresponding to the low- and high-temperature ranges of 226 and 284 K are shown in Figures S3 and S4, respectively, in the supporting information.

The averaged densities for each L_s bin shown in Figure 6 at subsolar conditions and the corresponding empirical temperatures described in this work are used to generate the estimated escape rates for deuterium (Jeans, 1925). The resulting escape rates are listed in Table 2 for the low-, average-, and high-temperature cases of 226, 255, and 284 K, respectively.

5. Discussion

There is generally good agreement between observed and simulated D brightness values at perihelion conditions, as shown in Figures 5, S1, and S2). MAVEN arrived at Mars in September 2014, during perihelion of Mars Year (MY) 32. In the early IUVS measurements, echelle observations were made with relatively short integration times (few seconds) that introduced higher uncertainties than longer-integration observations later in the mission (MY 33 and beyond). A few cases in Figure 5 show a model-data divergence at lower altitudes (namely, in the southern hemisphere, $L_s = 240^{\circ}$ – 260° , SZA = 45° though 75° bins). The data from these bins are predominantly obtained from early mission data and the data-model discrepancy is likely associated with early echelle observational limitations (Mayyasi, Clarke, Bhattacharyya, et al., 2017). Additionally, model profiles agree better with the observations when temporally similar observations are used for co-

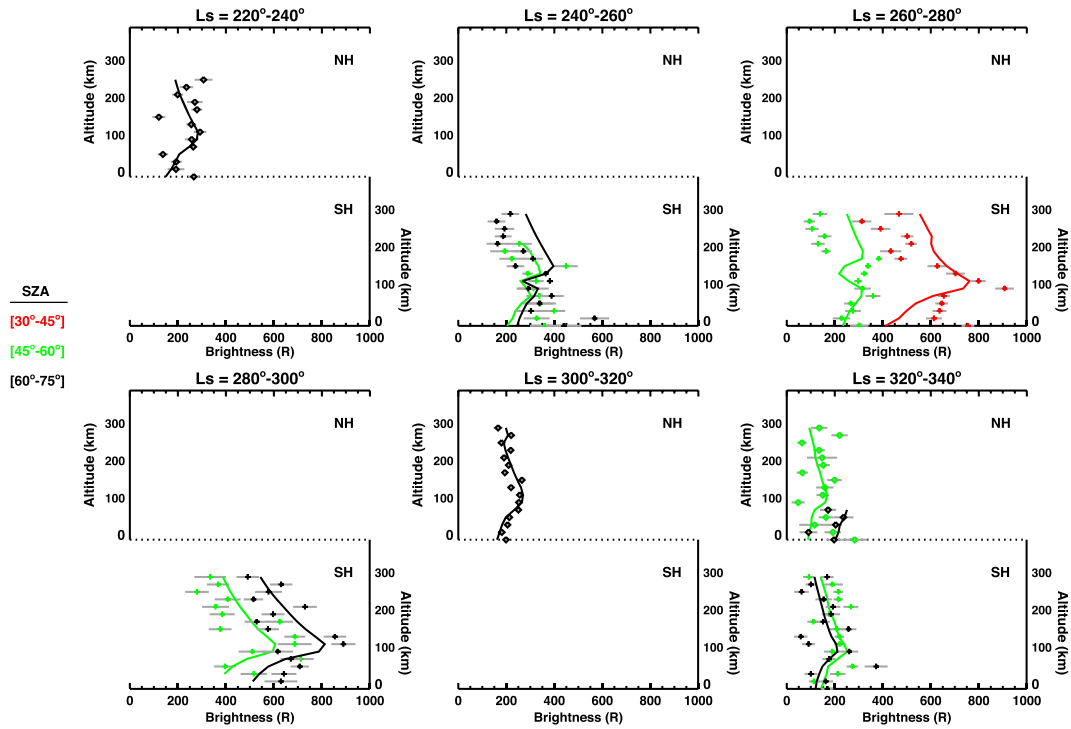


Figure 5. Deuterium brightness profiles derived from bin-specific co-added spectra, shown as a function of L_s (by panel), SZA (by color of profile), and adjacent hemispheres for comparison. Northern hemisphere profiles are shown on the top part of each panel as diamonds with an altitude scale on the top left of each panel. Southern hemisphere profiles are shown on the bottom part of each panel as crosses with an altitude scale on the bottom right of each panel. Season spans through perihelion with top rows covering (left) 220°–240°, (middle) 240°–260°, and (right) 260°–280°, respectively. Bottom row panels cover seasonal ranges of (left) 280°–300°, (middle) 300°–320°, and (right) 320°–340°, respectively. Data are shown in diamonds for SZAs spanning 30°–45° (red), 45°–60° (green), and 60°–75° (black). Uncertainties in the data points are shown in gray horizontal lines. Model fits to the data are shown as solid lines with the SZA-respective color code. In each panel, both northern hemisphere and southern hemisphere data and model plots follow the bottom scale for brightness in Rayleigh.

adding. This is because there is less variability in the ambient atmosphere along the line-of-sight vector used to generate the background atmosphere as well as less variability in the input solar EUV flux.

The D emission brightness increased as Mars approached perihelion and decreased as Mars moved further away from the Sun. These trends are similar in both hemispheres. When global data were available (in L_s bins 280°–300° and 320°–340°), northern hemispheric D brightness observations were comparable to or

Table 1

Modeled D Number Density at the Exobase (200 km) for the Observations Shown in Figure 5, and Extrapolated to Subsolar Point Conditions (SZA; $\chi = 0^\circ$) Using the Averaged Perihelion Temperature of 255 K

L_s Range	SZA Range	T_{exo} (K)	D_{exo} ($\times 10^3 \text{ cm}^{-3}$)	$\chi = 0^\circ T_{\text{exo}}$ (K)	$\chi = 0^\circ D_{\text{exo}}$ ($\times 10^3 \text{ cm}^{-3}$)
Northern Hemisphere					
220°–240°	60°–75°	232 ± 4	1.2 ± 0.18	248	1.0 ± 0.1
300°–320°	60°–75°	226 ± 6	1.5 ± 0.23	241	1.3 ± 0.1
320°–340°	45°–60°	227 ± 3	1.0 ± 0.26	237	0.8 ± 0.2
320°–340°	60°–75°	223 ± 4	2.4 ± 0.62	239	2.0 ± 0.4
Southern Hemisphere					
240°–260°	45°–60°	243 ± 3	1.0 ± 0.14	253	0.9 ± 0.1
240°–260°	60°–75°	237 ± 5	1.2 ± 0.19	253	1.0 ± 0.1
260°–280°	30°–45°	244 ± 3	2.3 ± 0.19	250	2.2 ± 0.1
260°–280°	45°–60°	241 ± 3	1.1 ± 0.16	251	1.0 ± 0.1
280°–300°	45°–60°	236 ± 2	2.4 ± 0.29	247	2.2 ± 0.2
280°–300°	60°–75°	230 ± 4	3.9 ± 0.54	246	3.3 ± 0.3
320°–340°	45°–60°	226 ± 3	1.5 ± 0.29	237	1.3 ± 0.2
320°–340°	60°–75°	221 ± 5	1.2 ± 0.33	238	1.0 ± 0.2

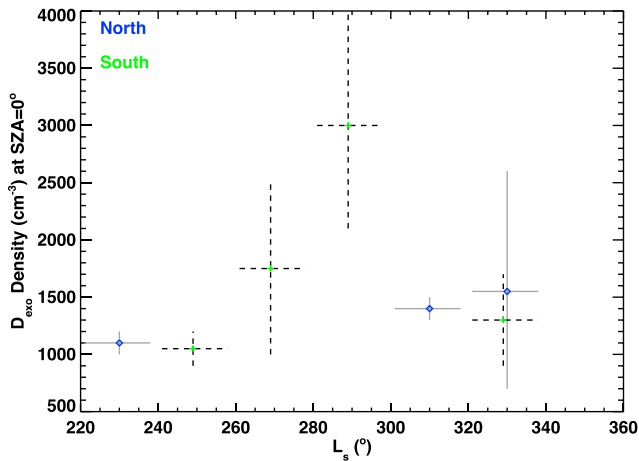


Figure 6. Deuterium density at the exobase, extrapolated to 0° SZA, constrained by data and model results at other SZA for perihelion conditions (220° to 340° L_s). The northern hemisphere data points (blue diamonds) and the southern hemisphere data points (green crosses) are shown with their uncertainties in solid gray and dashed black lines, respectively. The modeled results correspond to data averaged over a 20° range in L_s , indicated by the length of the horizontal uncertainties. The modeled density uncertainties (vertical lines) in each L_s bin correspond to the largest range of results from constraining the model to observed data at the observation's SZA bins. Data points from the southern hemisphere are offset by 1° in L_s from center of bin for clarity when shown along overlapping northern hemisphere data points.

brighter than southern hemispheric observations at similar seasonal epochs. In most of the subpanels in Figure 5 with brightness profiles, more than one profile with SZA was available. The observed brightness profiles show increasing, constant, and decreasing trends with increasing SZA. Theoretical estimates of these trends predict an enhancement in D brightness with decreasing SZA. The present data coverage is too sparse to empirically analyze these trends, and so further interpretation of D brightness variability with SZA is deferred to future work once more observations near perihelion become available.

The NGIMS temperatures at the exobase were derived with 1-sigma uncertainties with lower and higher limits of 226 and 284 K, respectively, at perihelion. A similar analysis was done at those temperature limits (with results shown in the supporting information). The resulting trends in brightness profiles, model fits, exobase densities, and escape rates for observational conditions as well as extrapolated subsolar conditions were consistent with the trends found at the average temperature of 255 K.

Modeled values of D density at the exobase altitude of 200 km are derived for the binned observational conditions, with the caveat of having no hemispherical differences in the empirical background neutral atmosphere. These values are extrapolated to subsolar conditions for more direct comparisons by hemisphere, as shown in Figures 6, S3, and S4). The exobase densities show similar trends in each hemisphere, with the northern hemisphere concentrations being comparable to and higher than concentrations in the southern hemisphere. Trends in the exobase density of both hemispheres peak near southern summer solstice (L_s

~280°–300° range). Simulating the observed D brightness with different temperatures for the northern and southern hemispheres may produce different densities. The 3-D temperature models validated to ongoing observations of the upper atmosphere would be useful for making these determinations in future work. The temperature values derived for the observational conditions and their subsequent modeled densities at the exobase are shown in Tables 1, S1, and S2). These tables also include D exobase densities extrapolated for subsolar conditions. Southern hemisphere-derived exobase temperatures do not vary from northern hemisphere temperatures, as expected from the atmospheric model assumptions.

In averaging the results of this work from both hemispheres, the D density at the exobase varies from $\sim 1 \times 10^3 \text{ cm}^{-3}$ at 220° L_s to $\sim 3 \times 10^3 \text{ cm}^{-3}$ at 280° L_s and then decreases to $\sim 1 \times 10^3 \text{ cm}^{-3}$ at 320° L_s for the average exobase temperature of 255 K. No other existing measurements of D densities near perihelion have been published to date for comparison to these results; however, theoretical estimates have been made. Previous modeling work derived an exobase density of $\sim 0.04 \times 10^3 \text{ cm}^{-3}$ at a higher temperature limit

Table 2
Modeled Jeans Escape Rates at Perihelion

L_s Range	$\chi = 0^\circ$ Jeans Escape Rate ($\times 10^3 \text{ atoms}\cdot\text{cm}^{-2}\cdot\text{s}^{-1}$)		
Northern Hemisphere			
	Low T Limit (226 K)	Average T (255 K)	High T Limit (284 K)
220°–240°	1.1 ± 0.1	4.7 ± 0.5	16 ± 1.6
300°–320°	0.9 ± 0.0	4.6 ± 0.4	15 ± 1.3
320°–340°	0.8 ± 0.5	4.6 ± 2.7	17 ± 11
Southern Hemisphere			
	Low T Limit (226 K)	Average T (255 K)	High T Limit (284 K)
240°–260°	1.6 ± 0.2	5.7 ± 0.9	16 ± 1.7
260°–280°	2.2 ± 1.0	8.6 ± 3.8	25 ± 9.8
280°–300°	2.9 ± 0.9	13 ± 3.6	37 ± 10
320°–340°	0.6 ± 0.2	3.4 ± 1.0	12 ± 3.5

(~ 350 K) than used here (Yung et al., 1988). A subsequent study derived a modeled exobase density of $\sim 0.5 \times 10^3 \text{ cm}^{-3}$ for a temperature comparable to the average case here (Krasnopolsky, 2002). More recently, a theoretical model analyzing lower resolution (FUV) IUVS observations made during December 2014 and August 2016 computed a D exobase density of $\sim 2 \times 10^3 \text{ cm}^{-3}$ at $L_s \sim 205^\circ$ for a temperature of ~ 185 K, and $\sim 5 \times 10^3 \text{ cm}^{-3}$ at $L_s \sim 255^\circ$ and temperature of ~ 265 K, respectively (Chaffin et al., 2018). These theoretical results compare favorably within the limits of the observations and simulations found in this work for the average temperature range and are consistent with the higher and lower limit temperature results shown in the Tables S1 and S2 in the supporting information where the temperatures are closer to those modeled from FUV data.

The Jeans escape rate was calculated for aphelion conditions (as an upper limit) and for 20° seasonal bins at perihelion conditions. The trends in escape rate near perihelion follow those of D exobase density at 0° SZA and brightness at the observed conditions. The uncertainties in the escape rates are representative of those of the extrapolated densities at the assumed exobase temperatures described in Table 2. The D escape rate at the exobase for the average temperature conditions determined here varies seasonally within the range of ~ 2 – $19 \times 10^3 \text{ atoms}\cdot\text{cm}^{-2}\cdot\text{s}^{-1}$ in the southern hemisphere. At the low temperature limit, these seasonal variations span ~ 0.5 – $4 \times 10^3 \text{ atoms}\cdot\text{cm}^{-2}\cdot\text{s}^{-1}$. At the high temperature limit, the southern hemisphere seasonal variations span ~ 9 – $47 \times 10^3 \text{ atoms}\cdot\text{cm}^{-2}\cdot\text{s}^{-1}$.

Interhemispheric deuterium escape rate comparisons are limited by observations. There is insufficient coverage of northern hemisphere observations near perihelion at the time of this work to compare trends in escape rates, and from existing coverage, would seem to be constant. Escape rates for the northern hemisphere vary from ~ 1 , to ~ 4.5 , to $\sim 16 \times 10^3 \text{ atoms}\cdot\text{cm}^{-2}\cdot\text{s}^{-1}$ for low-, average-, and high-temperature conditions, respectively, and seem relatively stable across the observed L_s ranges. The variation in escape rate across temperature limits and observed L_s range span an order of magnitude both hemispheres.

Previous theoretical models estimated a deuterium escape rate of ~ 8 – $15 \times 10^3 \text{ atoms}\cdot\text{cm}^{-2}\cdot\text{s}^{-1}$ at temperature conditions similar to the average temperature adopted here (Krasnopolsky, 2002), and $\sim 7 \times 10^3 \text{ atoms}\cdot\text{cm}^{-2}\cdot\text{s}^{-1}$ at higher temperatures than the high temperature limit obtained here (Yung et al., 1988). Analysis of ongoing and future MAVEN observations would enable further determinations of D abundances, escape rates, and their variability across hemispheres and seasonal coverage.

6. Interpretation

The simulated trends of D densities and escape rates are consistent with observed and theoretical expectations of Lyman- α brightness variations with Martian season. The global mean temperature in the exosphere of Mars is higher at perihelion than at aphelion, and D irradiances were found to increase as Mars approaches the Sun in its orbit. It is plausible that seasonal drivers produce circulation patterns in the lower atmosphere that cause an upwelling of water and its deuterated constituents into higher altitudes when Mars is closer to the Sun.

The increasing and decreasing trends in D properties near perihelion occur during the dust season at Mars ($L_s \sim 220^\circ$ – 330°). Type A and C dust storms originate in the northern hemisphere and migrate south (Fernández, 1998). The dynamics of dust migration and circulation contribute to transporting water from the surface to higher altitudes (Heavens et al., 2018). Additional weather circulation patterns distribute photo-dissociated water products from these altitudes into the upper atmosphere (e.g., Clarke, 2018), and may do so with varying efficiency in the hemisphere of dust storm origin. At the time of this writing, Mars is experiencing a planet encircling dust event. Analysis of MAVEN IUVS echelle observations for this time and over the subsequent few months would contribute to determining the effects of dust storms on the variability of D and H properties and their escape rates in the upper atmosphere of Mars.

These seasonal trends in D densities are global since they are consistent for both hemispheres. Similar trends have been found for properties of upper atmospheric hydrogen at Mars (Bhattacharyya et al., 2015; Clarke et al., 2014, 2017; Halekas, 2017). Studies of water variability lower in the atmosphere, using spectral analysis of H_2O and HDO as well as using simulations, have shown seasonal differences in the distribution of water and its isotopologues lower in the Martian atmosphere (Encrenaz et al., 2016; Encrenaz et al., 2018; Fedorova et al., 2018; Krasnopolsky, 2015; Montmessin et al., 2005; Villanueva et al., 2015).

The surface in the northern hemisphere of Mars has been found to be as ancient as that in the southern hemisphere, estimated from underground crater detections (Watters et al., 2006). Geological fluvial activity, attributed to covering up many of these craters in the northern hemisphere, is associated with an enhanced reservoir for subsurface H₂O and HDO (Orosei et al., 2018). The water cycle at Mars includes these reservoirs as sources for upper atmospheric deuterium (Bertaux & Montmessin, 2001). Such a resource would plausibly contribute to asymmetric D abundances with hemisphere (Heavens et al., 2018).

Seasonal processes that produce a near threefold brightening in deuterium emission on a planet-wide scale are inferred to produce factors of three enhancements in exobase densities and escape rates in the southern and northern hemispheres. Within the limitations of data coverage, these trends appear symmetric about southern summer solstice. The D densities and escape rates found here by analysis of the MAVEN IUVS echelle observations are comparable to previous theoretical estimates at similar seasonal times. At overhead Sun conditions, the D exobase density ranges between ~ 1 and $4 \times 10^3 \text{ cm}^{-3}$. Extrapolating this density to lower altitudes using a simplified atmospheric model described in Matta (2013) produces a volume mixing ratio for deuterium that ranges between 4 and 22 parts per billion at 80 km for the average temperature conditions used here.

Deriving H densities from these observations requires more comprehensive transfer modeling to account for the optically thick emission. Efforts are underway to do so in order to derive and interpret the D/H ratio and its variability in the upper atmosphere of Mars. Based on the results of this analysis, the properties of D and H are expected to vary with altitude from the surface to space as well as with season. The variations in D densities in the upper atmosphere presented in this work will complement derivations of the D/H ratio in the lower atmosphere of Mars (below 80 km) made by the Trace Gas Orbiter mission (Korablev et al., 2018; Vandaele, 2018). As more perihelion observations become available, variations due to hemispherical processes may become more apparent. This variability would provide new insights into the hydrological cycle at Mars; the effects of dust activity on regional and global water escape and would be helpful in constraining primordial water content at the planet.

Acknowledgments

The first author thanks Paul Withers for discussions of reference frames within the MAVEN instrument suite, Jean-Loup Bertaux for insights into spectral instrument limitations, and two anonymous reviewers for their helpful comments. This work was supported, in part, by NASA grant 80NSSC18K0266 and by NASA contract 1000320450 from the University of Colorado to Boston University. J.-Y.C. is funded by the program 'Système Solaire' of Centre National d'Études Spatiales. The MAVEN data used here are available on the NASA Planetary Data System at <https://pds.nasa.gov/datasearch/subscription-service/SS-20180215.shtml> for release 12 of the IUVS level1a and level1c echelle data set.

References

- Benna, M., Mahaffy, P. R., Grebowsky, J. M., Fox, J. L., Yelle, R. V., & Jakosky, B. M. (2015). First measurements of composition and dynamics of the Martian ionosphere by MAVEN's neutral gas and ion mass spectrometer. *Geophysical Research Letters*, *42*, 8958–8965. <https://doi.org/10.1002/2015GL066146>
- Bertaux, J. L., Clarke, J., Mumma, M., Owen, T., & Quémérais, E. (1993). A search for the deuterium Lyman-alpha emission from the atmosphere of Mars, in Science with the Hubble Space Telescope, ESO proc. No. 44, 459.
- Bertaux, J. L., Goutail, F., Dimarellis, E., Kockarts, G., & Van Ransbeeck, E. (1984). First optical detection of atomic deuterium in the upper atmosphere from Spacelab1. *Nature*, *309*(5971), 771–773. <https://doi.org/10.1038/309771a0>
- Bertaux, J.-L., Korablev, O., Perrier, S., Quémérais, E., Montmessin, F., Leblanc, F., Lebonnois, S., et al. (2006). SPICAM on Mars Express: Observing modes and overview of UV spectrometer data and scientific results. *Journal of Geophysical Research*, *111*, E10S90. <https://doi.org/10.1029/2006JE002690>
- Bertaux, J.-L., & Montmessin, F. (2001). Isotopic fractionation through water vapor condensation: The Deuteropause, a cold trap for deuterium in the atmosphere of Mars. *Journal of Geophysical Research*, *106*(E12), 32,879–32,884. <https://doi.org/10.1029/2000JE001358>
- Bhattacharyya, D., Clarke, J. T., Bertaux, J.-L., Chaufray, J.-Y., & Mayyasi, M. (2015). A strong seasonal dependence in the Martian hydrogen exosphere. *Geophysical Research Letters*, *42*, 8678–8685. <https://doi.org/10.1002/2015GL065804>
- Bhattacharyya, D., Clarke, J. T., Bertaux, J.-L., Chaufray, J.-Y., & Mayyasi, M. (2017). Analysis and modeling of remote observations of the Martian hydrogen exosphere. *Icarus*, *281*, 264–280. <https://doi.org/10.1016/j.icarus.2016.08.034>
- Bhattacharyya, D., Clarke, J. T., Chaufray, J. Y., Mayyasi, M., Bertaux, J. L., Chaffin, M. S., Schneider, N. M., et al. (2017). Seasonal changes in hydrogen escape from Mars through analysis of HST observations of the Martian exosphere near perihelion. *Journal of Geophysical Research: Space Physics*, *122*, 11,756–11,764. <https://doi.org/10.1002/2017JA024572>
- Bibring, J.-P., Langevin, Y., Mustard, J., Poulet, F., Arvidson, R., Gendrin, A., Gondet, B., et al., & the OMEGA team (2006). Global mineralogical and aqueous Mars history derived from OMEGA/Mars Express Data. *Science*, *312*(5772), 400–404. <https://doi.org/10.1126/science.1122659>
- Bougher, S. W., Roeten, K. J., Olsen, K., Mahaffy, P. R., Benna, M., Elrod, M., Jain, S. K., et al. (2017). The structure and variability of Mars dayside thermosphere from MAVEN NGIMS and IUVS measurements: Seasonal and solar activity trends in scale heights and temperatures. *Journal of Geophysical Research: Space Physics*, *122*, 1296–1313. <https://doi.org/10.1002/2016JA023454>
- Carr, M. (1986). Mars: A water-rich planet? *Icarus*, *68*(2), 187–216. [https://doi.org/10.1016/0019-1035\(86\)90019-9](https://doi.org/10.1016/0019-1035(86)90019-9)
- Chaffin, M., Chaufray, J.-Y., Deighan, J., Schneider, N., Mayyasi, M., Clarke, J., et al. (2018). Mars H escape rates derived from MAVEN/IUVS Lyman alpha brightness measurements and their dependence on model assumptions. *Journal of Geophysical Research: Planets*, *123*, 2192–2210. <https://doi.org/10.1029/2018JE005574>
- Chaffin, M., Deighan, J., Schneider, N., & Stewart, I. (2017). Elevated atmospheric escape of hydrogen from Mars induced by high-altitude water. *Nature Geoscience*, *10*(3), 174–178. <https://doi.org/10.1038/ngeo2887>
- Chaffin, M. S., Chaufray, J. Y., Deighan, J., Schneider, N. M., McClintock, W. E., Stewart, A. I. F., Thiemann, E., et al. (2015). Three-dimensional structure in the Mars H corona revealed by IUVS on MAVEN. *Geophysical Research Letters*, *42*, 9001–9008. <https://doi.org/10.1002/2015GL065287>

- Chaffin, M. S., Chaufray, J.-Y., Stewart, I., Montmessin, F., Schneider, N., & Bertaux, J.-L. (2014). Unexpected variability of Martian hydrogen escape. *Geophysical Research Letters*, *41*, 314–320. <https://doi.org/10.1002/2013gl058578>
- Chaufray, J. Y., Bertaux, J. L., LeBlanc, F., & Quemerais, E. (2008). Observation of the hydrogen corona with SPICAM on Mars express. *Icarus*, *195*(2), 598–613. <https://doi.org/10.1016/j.icarus.2008.01.009>
- Chaufray, J.-Y., Gonzalez-Galindo, F., Forget, F., Lopes-Valverde, M., Leblanc, F., Modolo, R., & Hess, S. (2015). Variability of the hydrogen in the Martian upper atmosphere as simulated by a 3D atmosphere-exosphere coupling. *Icarus*, *245*, 282–294.
- Chaufray, J.-Y., Yelle, R. V., Gonzalez-Galindo, F., Forget, F., Lopez-Valverde, M., LeBlanc, F., & Modolo, R. (2018). Effect of the lateral exospheric transport on the horizontal hydrogen distribution near the exobase of Mars. *Journal of Geophysical Research: Space Physics*, *123*, 2441–2454. <https://doi.org/10.1002/2017JA025163>
- Clarke, J. (2018). Dust-enhanced water escape. *Nature*, *2*(2), 114–115. <https://doi.org/10.1038/s41550-018-0383-6>
- Clarke, J. T., Bertaux, J.-L., Chaufray, J.-Y., Gladstone, G. R., Quemerais, E., Wilson, J. K., & Bhattacharyya, D. (2014). A rapid decrease of the hydrogen corona of Mars. *Geophysical Research Letters*, *41*, 8013–8020. <https://doi.org/10.1002/2014GL061803>
- Clarke, J. T., Mayyasi, M., Bhattacharyya, D., Schneider, N. M., McClintock, W. E., Deinghan, J. L., et al. (2017). Variability of D and H in the Martian upper atmosphere observed with the MAVEN IUVS echelle channel. *Journal of Geophysical Research: Space Physics*, *122*, 2336–2344. <https://doi.org/10.1002/2016JA023479>
- Cui, J., Yelle, R., Vuitton, V., Waite, J., Kasprzak, W., Gell, D., Niemann, H., et al. (2009). Analysis of Titan's neutral upper atmosphere from Cassini ion neutral mass spectrometer measurements. *Icarus*, *200*(2), 581–615. <https://doi.org/10.1016/j.icarus.2008.12.005>
- Ehlmann, B., & Edwards, C. (2014). Mineralogy of the Martian surface. *Annual Review of Earth and Planetary Sciences*, *42*(1), 291–315. <https://doi.org/10.1146/annurev-earth-060313-055024>
- Emerich, C., Lemaire, P., Vial, J.-C., Curdt, W., Schuhle, U., & Klaus, W. (2005). A new relation between the central spectral solar H I Lyman α irradiance and the line irradiance measured by SUMER/SOHO during the cycle 23. *Icarus*, *178*(2), 429–433. <https://doi.org/10.1016/j.icarus.2005.05.002>
- Encrenaz, T., DeWitt, C., Richter, M., Greathouse, T., Fouchet, T., Montmessin, F., Lefèvre, F., et al. (2018). New measurements of D/H on Mars using EXES aboard SOFIA. *Astronomy & Astrophysics*, *612*, A112. <https://doi.org/10.1051/0004-6361/201732367>
- Encrenaz, T., DeWitt, C., Richter, M., Greathouse, T., Fouchet, T., Montmessin, F., Lefèvre, F., et al. (2016). A map of D/H on Mars in the thermal infrared using EXES aboard SOFIA. *Astronomy & Astrophysics*, *586*, A62. <https://doi.org/10.1051/0004-6361/201527018>
- Eparvier, F., Chamberlin, P., Woods, T., & Thiemann, E. (2015). The solar extreme ultraviolet monitor for MAVEN. *Space Science Reviews*, *195*(1–4), 293–301. <https://doi.org/10.1007/s11214-015-0195-2>
- Fedorova, A., Bertaux, J.-L., Betsis, D., Montmessin, F., Korabiev, O., Maltagliati, L., & Clarke, J. (2018). Water vapor in the middle atmosphere of Mars during the 2007 global dust storm. *Icarus*, *300*, 440–457. <https://doi.org/10.1016/j.icarus.2017.09.025>
- Fernández, W. (1998). Martian dust storms: A review. *Earth, Moon, and Planets*, *77*, 19–46.
- Fisher, D. A. (2007). Mars' water isotope (D/H) history in the strata of the north polar cap: Inferences about the water cycle. *Icarus*, *187*(2), 430–441. <https://doi.org/10.1016/j.icarus.2006.10.032>
- Forget, F., Hourdin, F., Fournier, R., Hourdin, C., Talagrand, O., Collins, M., Lewis, S. R., et al. (1999). Improved general circulation models of the Martian atmosphere from the surface to above 80 km. *Journal of Geophysical Research*, *104*(E10), 24,155–24,175. <https://doi.org/10.1029/1999JE001025>
- Gillmann, C., Lognonné, P., & Moreira, M. (2011). Volatiles in the atmosphere of Mars: The effects of volcanism and escape constrained by isotopic data. *Earth and Planet Science Letters*, *303*(3–4), 299–309. <https://doi.org/10.1016/j.epsl.2011.01.009>
- Halekas, J. (2017). Seasonal variability of the hydrogen exosphere of Mars. *Journal of Geophysical Research: Planets*, *122*, 901–911. <https://doi.org/10.1002/2017JE005306>
- Head, J., Mustard, J., Kreslavsky, M., Milliken, R., & Marchant, D. (2003). Recent ice ages on Mars. *Nature*, *426*(6968), 797–802. <https://doi.org/10.1038/nature02114>
- Heavens, N., Kleinböhl, A., Chaffin, M., Halekas, J., Kass, D., Hayne, P., McCleese, D., et al. (2018). Hydrogen escape from Mars enhanced by deep convection in dust storms. *Nature*, *2*(2), 126–132. <https://doi.org/10.1038/s41550-017-0353-4>
- Hodges, R. J. R., & Johnson, F. (1968). Lateral transport in planetary exospheres. *Journal of Geophysical Research*, *73*(23), 7307–7317. <https://doi.org/10.1029/JA073i023p07307>
- Horner, J., Mousis, O., Petit, J.-M., & Jones, B. (2009). Differences between the impact regimes of the terrestrial planets: Implications for primordial D:H ratios. *Planetary and Space Science*, *57*(12), 1338–1345. <https://doi.org/10.1016/j.pss.2009.06.006>
- Hunten, D. M., & McElroy, M. B. (1970). Production and escape of hydrogen on Mars. *Journal of Geophysical Research*, *75*(31), 5989–6001. <https://doi.org/10.1029/JA075i031p05989>
- Jakosky, B. (2015). MAVEN explores the Martian upper atmosphere. *Science*, *350*(6261), 643. <https://doi.org/10.1126/science.aad3443>
- Jakosky, B., Pepin, R., Johnson, R., & Fox, J. (1994). Mars atmospheric loss and isotopic fractionation by solar-wind-induced sputtering and photochemical escape. *Icarus*, *111*(2), 271–288. <https://doi.org/10.1006/icar.1994.1145>
- Jakosky, B., Slipski, M., Benna, M., Mahaffy, P., Elrod, M., Yelle, R., Stone, S., et al. (2017). Mars' atmospheric history derived from upper-atmosphere measurements of $^{38}\text{Ar}/^{36}\text{Ar}$. *Science*, *355*(6332), 1408–1410. <https://doi.org/10.1126/science.aai7721>
- Jakosky, B. M., Brain, D., Chaffin, M., Curry, S., Deighan, J., Grebowsky, J., Halekas, J., et al. (2018). Loss of the Martian atmosphere to space: Present-day loss rates determined from MAVEN observations and integrated loss through time. *Icarus*, *315*, 146–157. <https://doi.org/10.1016/j.icarus.2018.05.030>
- Jeans, J. H. (1925). *The Dynamical Theory of Gases* (4th ed.). Cambridge, UK: Cambridge University Press.
- Kass, D., & Yung, Y. (1999). Water on Mars: Isotopic constraints on exchange between the atmosphere and surface. *Geophysical Research Letters*, *26*(24), 3656–3656.
- Korablev, O., Montmessin, F., Trokhimovskiy, A., Fedorova, A. A., Shakun, A. V., Grigoriev, A. V., Moshkin, B. E., et al. (2018). The Atmospheric Chemistry Suite (ACS) of three spectrometers for the ExoMars 2016 trace gas orbiter. *Space Science Reviews*, *214*(1), 7. <https://doi.org/10.1007/s11214-017-0437-6>
- Krasnopolsky, V. (2000). On the deuterium abundance on Mars and some related problems. *Icarus*, *148*(2), 597–602. <https://doi.org/10.1006/icar.2000.6534>
- Krasnopolsky, V. (2002). Mars' upper atmosphere and ionosphere at low, medium, and high solar activities: Implications for evolution of water. *Journal of Geophysical Research*, *107*(E12), 5128. <https://doi.org/10.1029/2001JE001809>
- Krasnopolsky, V. (2015). Variations of the HDO/H₂O ratio in the Martian atmosphere and loss of water from Mars. *Icarus*, *257*, 377–386. <https://doi.org/10.1016/j.icarus.2015.05.021>

- Krasnopolsky, V., Mumma, M., & Gladstone, G. (1998). Detection of atomic deuterium in the upper atmosphere of Mars. *Science*, 280(5369), 1576–1580. <https://doi.org/10.1126/science.280.5369.1576>
- Lammer, H., Chassefière, E., Karatekin, Ö., Morschhauser, A., Niles, P., et al. (2013). Outgassing history and escape of the Martian atmosphere and water inventory. *Space Science Reviews*, 174, 113–154. <https://doi.org/10.1007/s11214-012-9943-8>
- Lewis, S. R., Collins, M., Read, P. L., Forget, F., Hourdin, F., Fournier, R., Hourdin, C., et al. (1999). A climate database for Mars. *Journal of Geophysical Research*, 104(E10), 24,177–24,194. <https://doi.org/10.1029/1999JE001024>
- Mahaffy, P., & 33 coauthors (2014). The neutral gas and ion mass spectrometer on the Mars Atmosphere and Volatile Evolution Mission. *Space Science Reviews*, 195(1-4), 49–73. <https://doi.org/10.1007/s11214-014-0091-1>
- Mahaffy, P., Webster, C. R., Stern, J. C., Brunner, A. E., Atreya, S. K., Conrad, P. G., et al. (2015). The imprint of atmospheric evolution in the D/H of Hesperian clay minerals on Mars. *Science*, 347(6220), 412–414. <https://doi.org/10.1126/science.1260291>
- Mahaffy, P. R., Benna, M., Elrod, M., Yelle, R. V., Bougher, S. W., Stone, S. W., & Jakosky, B. M. (2015). Structure and composition of the neutral upper atmosphere of Mars from the MAVEN NGIMS investigation. *Geophysical Research Letters*, 42, 8951–8957. <https://doi.org/10.1002/2015GL065329>
- Matta, M., Withers, P., & Mendillo, M. (2013). The composition of Mars' topside ionosphere: Effects of hydrogen. *Journal of Geophysical Research: Space Physics*, 118, 2681–2693. <https://doi.org/10.1002/jgra.50104>
- Matta, M. M. (2013). *Modeling the Martian Ionosphere*, (PhD). Boston, MA: Boston University.
- Mayyasi, M., Bhattacharyya, D., Clarke, J., Catalano, A., Benna, M., Mahaffy, P., Thiemann, E., et al. (2018). Significant space weather impact on the escape of hydrogen from Mars. *Geophysical Research Letters*, 45, 8844–8852. <https://doi.org/10.1029/2018GL077727>
- Mayyasi, M., Clarke, J., Bhattacharyya, D., Deighan, J., Jain, S., Chaffin, M., Thiemann, E., et al. (2017). The variability of atmospheric deuterium brightness at Mars: Evidence for seasonal dependence. *Journal of Geophysical Research: Space Physics*, 122, 10,811–10,823. <https://doi.org/10.1002/2017JA024666>
- Mayyasi, M., Clarke, J., Quénerais, E., Katushkina, O., Bhattacharyya, D., Chaufray, J. Y., et al. (2017). IUVS echelle-mode observations of interplanetary hydrogen: Standard for calibration and reference for cavity variations between Earth and Mars during MAVEN cruise. *Journal of Geophysical Research: Space Physics*, 122, 2105–2089. <https://doi.org/10.1002/2016JA023466>
- McClintock, W., Schneider, N., Holsclaw, G., Clarke, J., Hoskins, A., Stewart, I., Montmessin, F., et al. (2015). The Imaging Ultraviolet Spectrograph (IUVS) for the MAVEN mission. *Space Science Reviews*, 195(1–4), 75–124. <https://doi.org/10.1007/s11214-014-0098-7>
- Montmessin, F., Fouchet, T., & Forget, F. (2005). Modeling the annual cycle of HDO in the Martian atmosphere. *Journal of Geophysical Research*, 110, E03006. <https://doi.org/10.1029/2004JE002357>
- Nagy, A., A. Balogh, T. Cravens, M. Mendillo, I. Müller-Wodarg (Eds.) (2009). *Mars Aeronomy*.
- Orosei, R., Lauro, S. E., Pettinelli, E., Cicchetti, A., Coradini, M., Cosciotti, B., di Paolo, F., et al. (2018). Radar evidence of subglacial liquid water on Mars. *Science*, eaar7268. <https://doi.org/10.1126/science.aaar7268> (2018)
- Owen, T. (1992). In H. Kieffer, B. Jakosky, C. Snyder, & M. Matthews (Eds.), *The Composition and Early History of the Atmosphere of Mars, Mars* (pp. 818–834). Tucson: University of Arizona Press.
- Smith, M., Wolff, M., Clancy, T., & Murchi, S. (2009). Compact Reconnaissance Imaging Spectrometer observations of water vapor and carbon monoxide. *Journal of Geophysical Research*, 114, E00D03. <https://doi.org/10.1029/2008JE003288>
- Solomon, S., Aharonson, O., Aurnou, J., Banerdt, W., Carr, M. H., Dombard, A. J., et al. (2005). New perspectives on Ancient Mars. *Science*, 307(5713), 1214–1220. <https://doi.org/10.1126/science.1101812>
- Stone, S., Yelle, R., Benna, M., Elrod, M., & Mahaffy, P. (2018). Thermal structure of the Martian upper atmosphere from MAVEN NGIMS. *Journal of Geophysical Research: Planets*, 123, 2842–2867. <https://doi.org/10.1029/2018JE005559>
- Stone, S., Yelle, R., Mahaffy, P., Benna, M., Elrod, M., & Bougher, S. (2016). Temperature variations in the Martian upper atmosphere from the MAVEN neutral gas and ion mass spectrometer, AAS DPS meeting #48, id.303.08.
- Thiemann, E. M. B., Chamberlin, P. C., Eparvier, F. G., Templeman, B., Woods, T. N., Bougher, S. W., Jakosky, B. M. (2017). The MAVEN EUVM model of solar spectral irradiance variability at Mars: Algorithms and results. *J. Geophys. Res.*, 122, 2748–2767, <https://doi.org/10.1002/2016JA023512>
- Trokhimovskiy, A., Fedorova, A., Korablev, O., Montmessin, F., Bertaux, J.-L., Rodin, A., & Smith, M. (2015). Mars' water vapor mapping by the SPICAM IR spectrometer: Five Martian years of observations. *Icarus*, 251, 50–64. <https://doi.org/10.1016/j.icarus.2014.10.007>
- Vandaele, A.-C. (2018). NOMAD, an integrated suite of three spectrometers for the ExoMars trace gas orbiter Mission: Technical description, science objectives and expected performance. *Space Science Reviews*, 214(5), 80. <https://doi.org/10.1007/s11214-018-0517-2>
- Vidal-Madjar, A., & Bertaux, J.-L. (1972). A calculated hydrogen distribution in the exosphere. *Planetary and Space Science*, 20(8), 1147–1162. [https://doi.org/10.1016/0032-0633\(72\)90004-9](https://doi.org/10.1016/0032-0633(72)90004-9)
- Villanueva, G. L., Mumma, M. J., Novak, R. E., Käufel, H. U., Hartogh, P., Encrenaz, T., et al. (2015). Strong water isotopic anomalies in the Martian atmosphere: Probing current and ancient reservoirs. *Science*, 348(6231), 218–221. <https://doi.org/10.1126/science.aaa3630>
- Watters, T., Leuschen, C., Plaut, J., Picardi, G., Safaenili, A., Clifford, S., Farrell, W., et al. (2006). MARSIS radar sounder evidence of buried basins in the northern lowlands of Mars. *Nature*, 444(7121), 905–908. <https://doi.org/10.1038/nature05356>
- Yung, Y., Wen, J.-S., Pinto, J., Allen, M., Pierce, K., & Paulson, S. (1988). HDO in the Martian atmosphere: Implications for the abundance of crustal water. *Icarus*, 76(1), 146–159. [https://doi.org/10.1016/0019-1035\(88\)90147-9](https://doi.org/10.1016/0019-1035(88)90147-9)